Materials Advances

ROYAL SOCIETY OF CHEMISTRY

PAPER

View Article Online
View Journal | View Issue

Check for updates

Cite this: *Mater. Adv.*, 2022, 3, 5064

# High content of hydrogenated pyridinic-N in a $SnO_2$/NGO heterogeneous material as an ultra-high sensitivity formaldehyde sensor†

Jing Lu, * Yajun Wang, Can Xu, Ying Zhang and Zijin Fu

Developing ultrasensitive materials with high selectivity and low detection limit has always been a challenge in the gas sensor field. In this work, $SnO_2$/N-doped graphene oxide (NGO) heterogeneous materials are prepared by a facile hydrothermal method. The different N-doped moieties in NGO play a very important role in regulating the microstructure and sensing properties of the composite. The results show that $SnO_2$/NGO with a high content of hydrogenated pyridinic-N exhibits excellent sensing performances towards formaldehyde. It shows good response linearity in the concentration range of 100–1000 ppb and 1–10 ppm. The actual detection limit is reduced to 100 ppb, and the response time and recovery time are 46 s and 63 s. The material shows high selectivity to formaldehyde, and the anti-interference coefficients are 8.6, 11.3, and 11.2 for ethanol, ammonia and acetone, respectively. The high selectivity and sensitivity of $SnO_2$/NGO are attributed to the following aspects: (i) large specific surface area and strong adsorption ability; (ii) selective adsorption originated from different activated regions of hydrogenated pyridinic-N; (iii) catalytic effect on redox reactions between HCHO and $O^-$ by the hydrogenated pyridinic-N structure; (iv) uniformly distributed heterojunctions facilitate carrier separation and transport.

Received 7th February 2022,
Accepted 6th May 2022

DOI: 10.1039/d2ma00132b

rsc.li/materials-advances

Open Access Article. Published on 26 May 2022. Downloaded on 2/8/2026 1:01:11 PM.
This article is licensed under a Creative Commons Attribution-NonCommercial 3.0 Unported Licence.

## Introduction

Formaldehyde (HCHO) is a common chemical reagent, which has been widely used in the textile, home decoration, medical, chemical and many other industries.[1,2] However, it is a toxic and harmful gas that has a strong effect on inducing abnormal immune functions, liver and central nervous system damage, respiratory illness and even cancers.[3,4] The World Health Organization (WHO) has proposed the maximum safe exposure concentration of formaldehyde for human life to be 80 ppb.[5,6] It is of great significance to detect formaldehyde vapor at the ppb level.

Tin dioxide ($SnO_2$) is an excellent semiconductor gas-sensing material, which exhibits high sensitivity, fast response and high stability to many kinds of volatile organic compounds.[7,8] However, the detection range of pure $SnO_2$ to HCHO is still concentrated in the ppm level.[1,9,10] For environmental monitoring and human health protection, the formaldehyde sensitivity needs to be further improved. In addition, a sensor's selectivity is very important because the real indoor air often contains several interfering gases.

In recent years, people have developed various methods to improve the sensitivity of $SnO_2$. In particular, heterogeneous materials[11–13] composed of $SnO_2$ and graphene-related materials have attracted much interest.[14–17] Graphene and its derivatives have large specific surface area, good conductivity and adjustable surface chemistry, and the related composites usually exhibit significantly enhanced sensitivity.[18,19] For example, the $SnO_2$/GO materials have lower working temperature than $SnO_2$ because of the good conductivity at low temperature.[14,15] The response value also can be improved such that the GO/hollow nanotube-like $SnO_2$ composite shows a 5 times higher value than $SnO_2$.[15] Wan *et al.* prepared a 3D-$SnO_2$ nanosheet/GO composite, which shows a response of 280 to 100 ppm formaldehyde at a working temperature of 60 °C.[16] Another $SnO_2$/GO with a mesoporous structure shows a much higher response of 2000 to 100 ppm formaldehyde at the same working temperature.[17] Considering the need for ppb level detection and high selectivity in actual detection, the sensitivity of the material deserves further improvement.

Nitrogen doped graphene has N atoms that interact with the $sp^2$ carbons *via* π–π interactions and donating electrons into graphene's matrix. N-doping can effectively change the spin

*School of Material Science and Engineering, International S&T Cooperation Foundation of Shaanxi Province, Xi'an Key Laboratory of Green Manufacture of Ceramic Materials, Key Laboratory of Auxiliary Chemistry and Technology for Chemical Industry, Ministry of Education, Shaanxi University of Science and Technology, Xi'an, 710021, China*

† Electronic supplementary information (ESI) available. See DOI: https://doi.org/10.1039/d2ma00132b



© 2022 The Author(s). Published by the Royal Society of Chemistry

Open Access Article. Published on 26 May 2022. Downloaded on 2/8/2026 1:01:11 PM.
This article is licensed under a Creative Commons Attribution-NonCommercial 3.0 Unported Licence.

density and charge distribution of adjacent carbon atoms, which results in more active sites for adsorption and tunable chemical and physical properties.[20,21] It also changes the bandgap and makes it possible to adjust the conductivity and the electronic behavior of graphene. Therefore, N-doped graphene has electrocatalytic activity,[22–25] particularly in the oxygen reduction reaction (ORR). Formaldehyde sensitivity involves the redox reaction between HCHO and $O_2$, which is closely related to the ORR.[1–3,9–13] It is supposed that N-doped graphene would improve selective adsorption and promote sensing reactions. So a highly sensitive $SnO_2$/NGO heterogeneous material deserves exploration and in-depth investigation.

Nitrogen-doped graphene shows different chemical structures possessing several forms of N moieties, such as graphitic-N, pyridinic-N, pyrrolic-N, hydrogenated pyridinic-N, amine N and so on.[26,27] Recently, there have been many research studies discussing the effect of N moieties on their sensing performances. It has been pointed out that N-doping could adjust the adsorption energy and the distance between doping atoms and gas molecules for the stable adsorption configurations.[28,29] Pyridinic-N has lone electron pairs and changes the charge transfer greatly. It exhibits excellent electrocatalytic and selective sensing performances.[26] Pyrrolic-N centers occur in $sp^2$-hybridized five-membered rings and show magnetic sensing effects.[26] Graphitic-N atoms facilitate electron transfer and could be the catalytic center of ORR reactions.[26] Hydrogenated pyridinic-N has gained interest since it is critical for enhancing adsorption and catalytic properties.[27,30] So far, it is still not clear which N doping structure is favorable for formaldehyde sensitivity.

Nitrogen-doped graphene composites can be prepared by many methods, such as chemical vapor deposition (CVD),[30] ball milling,[31] heat treatment,[32,33] hydrothermal,[34,35] chemical reduction[36] and plasma bombardment.[37] These fabrication techniques are highly effective in terms of doping. But the types and levels of incorporated N atoms cannot be well controlled. In this paper, $SnO_2$/NGO material with a high content of hydrogenated pyridinic-N moieties was prepared by adjusting the N-doping reagent in a hydrothermal process. The roles of different heterostructures towards formaldehyde sensing properties were investigated. It was observed that hydrogenated pyridinic-N can boost formaldehyde sensitivity by acting as the activated sites for adsorption and redox of formaldehyde and oxygen on the material surface. The as-prepared $SnO_2$/NGO shows high response and selectivity to formaldehyde at ppb level concentration. This work provides a controllable strategy for constructing $SnO_2$/NGO materials with different distributions of N-doped structures. And it suggests the hydrogenated pyridinic-N moiety as a vital microstructure in $SnO_2$/NGO for ultra-sensitive formaldehyde detection.

# Experimental

### Preparation of $SnO_2$/NGO heterogeneous materials

All reagents are of analytic grade and used without further purification. The $SnO_2$/NGO heterogeneous materials were prepared by a facile hydrothermal method. The N-doped microstructure of NGO was controlled by different doping processes using urea and ammonia hydrate as doping reagents.

In a typical synthesis, 11.3 mg graphene oxide was dispersed in deionized water with ultrasonic treatment to get a GO suspension. Then, 0.34 g $SnCl_2{\cdot}2H_2O$ and 0.32 g NaOH were added into the suspension to get a mixture. The nitrogen doping reagent was subsequently added dropwise into the mixture with constant stirring for 30 minutes at room temperature. Next, the mixture was transferred and sealed into a polytetrafluoroethylene lined kettle for hydrothermal reaction at 180 °C for 12 h. After reaction, the sample was cooled and filtered with deionized water and ethanol three times, respectively. The final product was collected and dried in a vacuum drying oven at 80 °C for 8 hours. The N-doping reagent dosage was 0.075 mol, pure urea was used for preparing the SNG-1 sample, and a mixture of urea and $NH_3{\cdot}H_2O$ with a molar mass ratio of 1 : 1 was used to obtain the SNG-2 sample. In addition, $SnO_2$ and $SnO_2$/GO(SG) were also prepared based on the same hydrothermal process for comparison.

### Characterizations

The XRD diffraction pattern of the prepared material was obtained using a D/max2200PC X-ray diffractometer. Raman spectroscopy was performed using a British Renishaw-invia micro-confocal laser Raman spectrometer. Thermogravimetric (TG) curves were obtained with a TGA2 instrument. A Thermo Scientific Escalab 250Xi photoelectron spectrometer was used to test the surface chemistry information of the material. A transmission electron microscope (TEM, Tecnai G2 F20 S-TWIN, FEI) and scanning electron microscope (SEM, S4800) were used to characterize the surface morphology and microstructure of the materials. A specific surface and porosity analyzer ASAP2460 of American Mike Instruments was used to detect the $N_2$ adsorption–desorption isotherm of the material to obtain its specific surface area and pore structure information. The impedance tests were performed using a CHI-660E electrochemical workstation.

### Fabrication and measurement of the gas sensor

The as-prepared material and the binder were mixed uniformly and then coated on a ceramic tube with a Pt electrode, and the working temperature was maintained at 160 °C through a heating resistor in the tube for 72 h to obtain stable sensitivity. Next, a certain concentration of target gas was introduced into the test system, and the change in resistance of the material in the air ($Ra$) and in the target gas ($Rg$) were measured to obtain the response and selectivity. The response ($S$) of the material is defined as $S = R_a/R_g$. The anti-interference coefficient $\kappa$ is defined as $\kappa = S_1/S_2$, where $S_1$ and $S_2$ are the response of the material to the target gas and interference gas, respectively.

### Adsorption kinetic study

The sensing material was firstly vacuum-dried to obtain a fresh surface for adsorption. Then the material was transferred into the target gas atmosphere with saturated vapor at certain

Open Access Article. Published on 26 May 2022. Downloaded on 2/8/2026 1:01:11 PM.
This article is licensed under a Creative Commons Attribution-NonCommercial 3.0 Unported Licence.

temperature. The adsorption amount is obtained by weighing the mass differences of the sensing materials before and after adsorption using an analytical balance, recording the adsorption amount of the material at different times, and drawing the adsorption isotherms. Then, we fit the adsorption amount per unit area of the material at different temperatures to get the slope $k$. And fit the data points obtained at the three temperatures for $\ln k$ and $1/T$ to get the slope $k^*$. According to the Arrhenius formula, the material's adsorption activation energy for the target gas can be calculated.

## Results and discussion

### Characterization

Fig. 1(a) shows the X-ray diffraction patterns of the $SnO_2$, SG, SNG-1 and SNG-2 sensing materials. It is clear that tetragonal rutile $SnO_2$ (JCPDS 41-1445) is obtained by the facile hydrothermal process. As for the heterogeneous materials, the composition does not change, but the $SnO_2$ crystallinity is reduced. This phenomenon is more obvious from SNG-1 and SNG-2. The grain sizes of $SnO_2$ in the different samples were further calculated by the Scherrer formula. The values are 37 nm, 25 nm, 12 nm, and 18 nm for $SnO_2$, SG, SNG-1 and SNG-2, respectively.[38,39] The addition of NGO helps to reduce the grain size of $SnO_2$ obviously, which may promote the adsorption ability of the SNGs owing to the increased specific surface area.

TG analysis was carried out to study the thermal stability and phase content of the composites. Fig. 1(c) shows that the weight loss of the materials can be divided into two stages. The first weight loss process is caused by the removal of surface adsorbed water below 100 °C.[22] The second weight loss during 300–650 °C is attributed to thermal decomposition of GO or NGO.[22,40] After 650 °C, the weight of the material remains stable and the remaining substance is $SnO_2$. So it can be concluded that the SG, SNG-1 and SNG-2 sensing materials exhibit good thermal stability below 300 °C. In addition, the $SnO_2$ content in SG, SNG-1 and SNG-2 was obtained as 95.2%, 94.3% and 94.4%, respectively.

The Raman spectra of the $SnO_2$, SG, SNG-1 and SNG-2 sensing materials are shown in Fig. 1(b). The peak at 632 $cm^{-1}$ corresponds to the semiconductor $SnO_2$, which proves the successful synthesis of $SnO_2$ in the composite. Compared with the SG sample, the D band of SNG shifts downward from 1580 $cm^{-1}$ to 1578 $cm^{-1}$, which indicates that N is doped into the lattice structure of GO.[17,41] The $I_D/I_G$ values, which suggest the lattice-defect density in the carbon materials, were calculated. The data shows an increase from SG to SNG materials because of the N doping. The difference between SNG-1 and SNG-2 is possibly from the different distribution of N-doped moieties.

Since the surface structure and chemical composition of sensing materials play a very important role in regulating the sensing performances, the materials were further characterized by X-ray photoelectron spectroscopy (XPS). Fig. 2(a) shows the O 1s spectrum. The strong peak at 531.5 eV is attributed to Sn–O bond,[17] and the small peak at 531.0 eV corresponds to the oxygen vacancies ($O_v$) of the $SnO_2$ crystal. When the $SnO_2$ was composited with GO or NGO, both the peaks shift to higher binding energy. That is caused by the formation of heterojunctions at the interface. A new peak at 532.6 eV corresponding to Sn–O–C bonds is also observed.[17] Compared to SG and SNG-1, the SNG-2 sample possesses more content of oxygen vacancies and Sn–O–C bonds, which may provide more active sites for formaldehyde adsorption and sensing reactions. The relative content of the O 1s spectrum is shown in Table S1 (ESI†). Fig. 2(b) shows the Sn 3d XPS spectra. The two peaks at 486.7 eV and 495.1 eV correspond to Sn $3d_{3/2}$ and Sn $3d_{5/2}$,[41,42] which

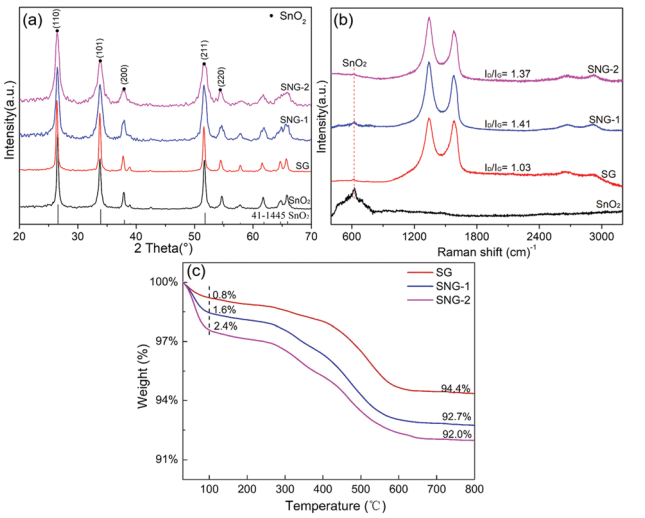


Fig. 1 XRD patterns (a) and Raman spectra (b) of the $SnO_2$, SG, SNG-1 and SNG-2 sensing materials, and (c) TG curves of SG, SNG-1 and SNG-2.

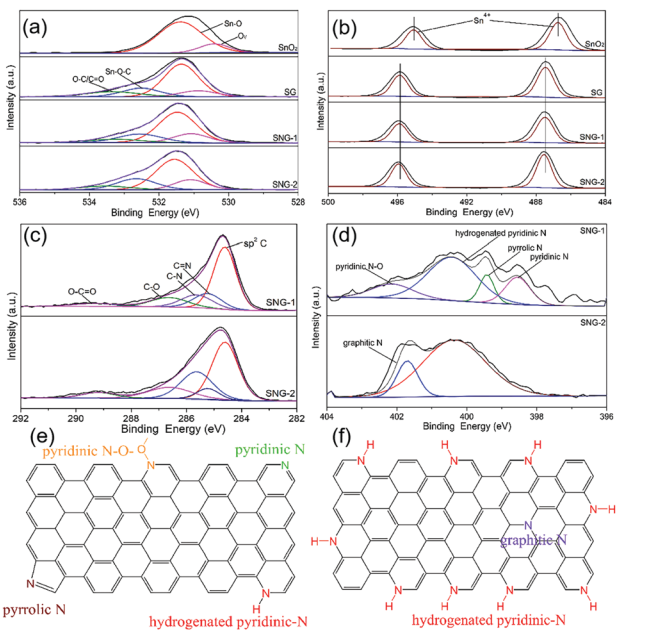


Fig. 2 XPS spectra of the $SnO_2$, SG, SNG-1 and SNG-2: (a) C 1s, (b) O 1s, (c) Sn 3d and (d) N 1s, and schematic diagram of the N-doped structure of (e) SNG-1, and (f) SNG-2.


© 2022 The Author(s). Published by the Royal Society of Chemistry

Open Access Article. Published on 26 May 2022. Downloaded on 2/8/2026 1:01:11 PM.
This article is licensed under a Creative Commons Attribution-NonCommercial 3.0 Unported Licence.

indicates Sn with the oxidation state of +4 valence. After composition, the Sn 3d peaks shifted toward a higher binding energy due to the formation of the Sn–O–C bond. For the SNG samples the shift tendency is much more obvious because of the N doping. This also indicates that there are more Sn–O–C bonds formed in the SNG-2 microstructure. Fig. 2(c) displays the C 1s spectra. It is clear that there are many oxygen-containing functional groups such as C–O bonds and C═O bonds in carboxyl groups from NGO. Compared to the SNG-2 sample, SNG-1 has more C═N bonds and less C–N bonds. This suggests that there are differences in the N-doped structure of the two SNG materials. The N spectrum presents more detailed information about the type and content of N moieties, which helps to understand the influence of structural change on the adsorption and sensing performance of SNG materials. Fig. 2(d) shows the existence of N in the SNG-1 and SNG-2 samples. For SNG-1, the N peak can be divided into four peaks at 398.5 eV, 399.4 eV, 400.5 eV and 402.2 eV, corresponding to pyridinic-N, pyrrolic-N, hydrogenated pyridinic-N and oxide pyridinic-N,[26,27] respectively. The relative contents of different N moieties is shown in Table S2 (ESI†), which are 18.1%, 10.8%, 55.9% and 15.2%, respectively. As for SNG-2, the N moiety distribution is quite different. The proportion of hydrogenated pyridinic-N increased dramatically, whereas the content of graphitic-N is very low. Such a unique difference is attributed to different doping processes caused by different nitrogen doping reagents. Generally, the volatilization rate of ammonia from $NH_3{\cdot}H_2O$ is higher than the thermal decomposition rate of urea into ammonia at the same temperature. So using $NH_3{\cdot}H_2O$ as part of the N-doped reagent will increase the doping speed or increase the N incorporation into GO. As a result, a number of hydrogenated pyridinic-N is generated at the edge of NGO. Whereas, urea is used as the only doping reagent for preparing SNG-1. The N-doping process is more uniform and gentle, so various N moieties such as pyridinic-N, pyrrolic-N, graphitic-N and oxide pyridinic-N are obtained. But the proportion of hydrogenated pyridinic-N in SNG-1 is relatively low. The specific nitrogen doping microstructures of SNG-1 and SNG-2 are illustrated in Fig. 2(e) and (f). The results show different types and distributions of N-doped moieties in SNG-1 and SNG-2, which may influence the adsorption and sensing reactions of the materials.

The morphology of the materials was further characterized. Fig. 3(a) shows an irregularly arranged flake morphology of pure $SnO_2$ particles. Fig. 3(b) shows that the average particle size of $SnO_2$ decreased significantly when it was composited with graphene oxide. This is consistent with many works that the presence of GO usually causes the inorganic particle size to decrease.[14,43] For SNG-1 and SNG-2, the $SnO_2$ particle size is further decreased, and the particle uniformity is obviously increased. Fig. 3(c) and (d) show that the $SnO_2$ from SNG-1 and SNG-2 exhibited more regular shape, smaller particle size, and better distribution on NGO. Fig. 3(e) and (f) are HRTEM images of SNG-1 and SNG-2, respectively. Two lattice fringes with an interplanar spacing of 0.33 nm and 0.24 nm are observed, which correspond to the (110) and (200) plane of

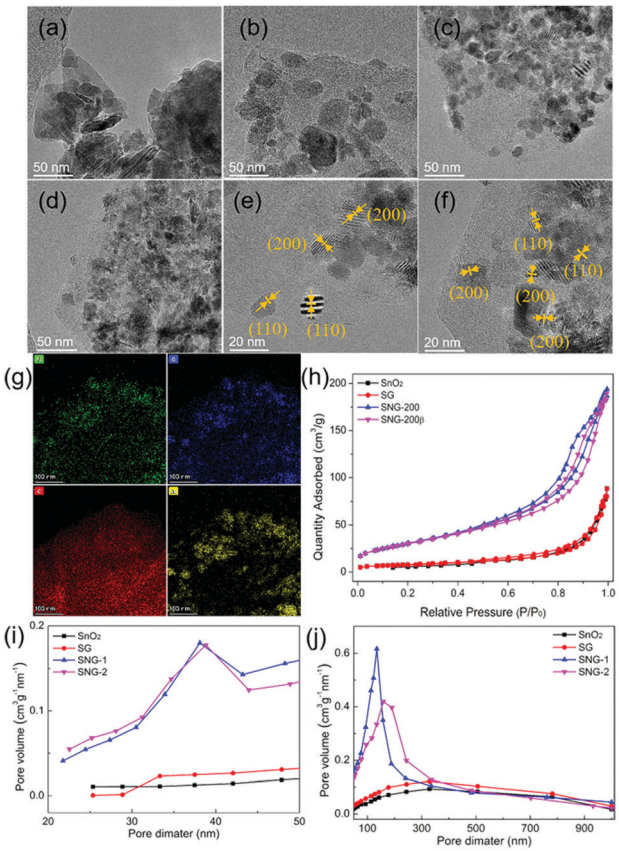


Fig. 3 TEM images of (a) $SnO_2$, (b) SG, (c) SNG-1 and (d) SNG-2, lattice fringes of (e) SNG-1 and (f) SNG-2, (g) EDS mapping of SNG-2, (h) $N_2$ adsorption/desorption isotherms, and pore diameter distribution in the range of (i) 0–50 nm and (j) 90–900 nm.

the $SnO_2$ phase.[17,44,45] The micro-area element distribution of the SNG-2 is shown in Fig. 3(g). The elements of O, C, N and Sn are distributed evenly, which indicates that $SnO_2$ is uniformly distributed on the NGO. Fig. 3(h) shows the adsorption/desorption isotherms of different sensing materials. Both SNG-1 and SNG-2 exhibit characteristic type-IV isotherms with a distinct hysteresis loop at high relative pressures, implying the presence of mesopores in the frameworks. Fig. 3(i) and (j) show the pore distributions of different materials. It is obvious that there are mesoporous and macroporous structures coexisting in SNG-1 and SNG-2. The mesopore size is concentrated at 38 nm, and the macropore diameter is about 170–200 nm. The specific surface area of the samples is also calculated: $SnO_2$ (15.4 $m^2\ g^{-1}$), SG (28.2 $m^2\ g^{-1}$), SNG-1 (111.7 $m^2\ g^{-1}$) and SNG-2 (110.6 $m^2\ g^{-1}$). The SNG samples possess larger specific surface area and more uniform particle distributions.

## Sensing performances

The gas sensing performances of $SnO_2$, SG, SNG-1 and SNG-2 were systematically tested and the results are shown in Fig. 4. All the sensing materials show a characteristic n-type sensing behavior at the optimal working temperature of 160 °C (Fig. S1, ESI†). Fig. 4(a) presents the good linear relationship between formaldehyde concentration and response in the range of 1–10

Open Access Article. Published on 26 May 2022. Downloaded on 2/8/2026 1:01:11 PM. This article is licensed under a Creative Commons Attribution-NonCommercial 3.0 Unported Licence.

ppm. Samples SNG-1 and SNG-2 can even respond to formaldehyde at low concentrations of 100–1000 ppb. Among all the samples, SNG-2 exhibits the highest response.

Fig. 4(b) shows the dynamic response of the prepared materials to formaldehyde at 100–1000 ppb and 1–9 ppm, respectively. $SnO_2$ and SG cannot respond to formaldehyde less than 1 ppm. However, the detection limit of SNG-1 and SNG-2 dropped to 100 ppb, which is very close to the formaldehyde indoor safety concentration (80 ppb) certified by the WHO. In addition, the response and recovery time of SNGs are reduced; the data are shown in Table S3 (ESI†). Fig. 4(c) shows the selectivity of $SnO_2$, SG, SNG-1 and SNG-2 to the same concentration of formaldehyde, ethanol, ammonia and acetone. Compared with pure phase $SnO_2$, the response of SNG-1 and SNG-2 to formaldehyde increased from 5.07 to greater than 10. Meanwhile, the response to ethanol, ammonia, and acetone decreased slightly, which indicates the superior selectivity of SNG-1 and SNG-2. Furthermore, the anti-interference performance of different materials was studied. The anti-interference coefficient $\kappa$ represents the ratio of the material's response to the target gas to that of the interfering gas ($\kappa = S_{\text{formaldehyde}}/S_{\text{interference gas}}$). The higher the ratio, the stronger the anti-interference ability. The $\kappa$ values were calculated and are listed in Table 1. It is obvious that the $\kappa$ values of SNG-1 and SNG-2 are generally higher than those of $SnO_2$ and SG. Finally, the long term stability of SNG-1 and SNG-2 was studied in Fig. 4(d). In the very first 8 weeks of application, the response of the SNGs decreased slightly. After 8 weeks, the response value almost kept constant and still reached more than 95% of the initial value.

In summary, the SNG-2 sample exhibits superior sensing performance to ppb level concentration of formaldehyde. The response of SNG-2 to 100 ppb formaldehyde is 2.0, and the response/recovery time is 46/63 s. It also shows high selectivity

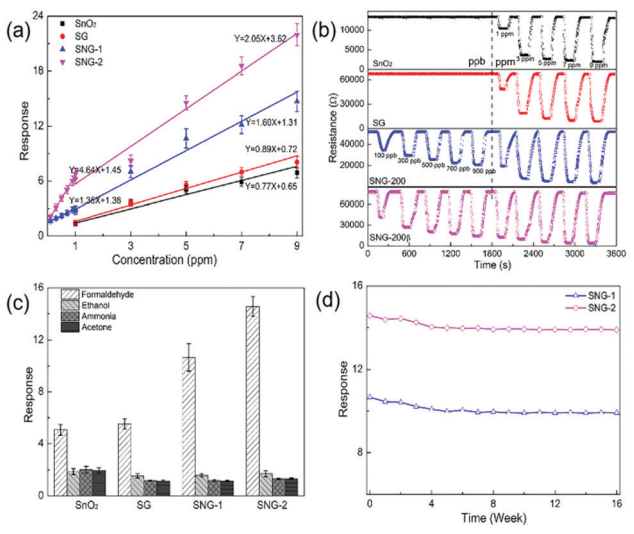


Fig. 4 (a) Sensing response of $SnO_2$, SG and SNG to formaldehyde in the range of 100–1000 ppb and 1–10 ppm, (b) the response–recovery curves, (c) the selectivity performances, and (d) the long-term stability of SNG-1 and SNG-2 to 5 ppm formaldehyde.

Table 1 Sensing response and anti-interference coefficient of the $SnO_2$, SG, SNG-1 and SNG-2 materials

| | $S_{HCHO}$ | $S_{C_2H_5OH}$ | $S_{NH_3}$ | $S_{C_3H_6O}$ | $\kappa_{C_2H_5OH}$ | $\kappa_{NH_3}$ | $\kappa_{C_3H_6O}$ |
|---|---|---|---|---|---|---|---|
| $SnO_2$ | 5.1 | 1.9 | 2.0 | 1.9 | 2.7 | 2.5 | 2.6 |
| SG | 5.6 | 1.5 | 1.2 | 1.1 | 3.6 | 4.7 | 4.8 |
| SNG-1 | 10.7 | 1.6 | 1.2 | 1.1 | 6.8 | 9.1 | 9.4 |
| SNG-2 | 14.6 | 1.7 | 1.3 | 1.3 | 8.6 | 11.3 | 11.2 |

and the anti-interference coefficient reaches 8.6–11.3 to ethanol, ammonia and acetone. In addition, the material exhibits excellent long-term stability. The overall performance suggests that the as-prepared $SnO_2$/SNG material is a promising sensitive material for indoor formaldehyde detection in the future. A summary of the related works is shown in Table S4 (ESI†). Compared with existing formaldehyde sensing materials based on $SnO_2$ and graphene derivatives, the SNG-2 has a much lower practical detection limit and higher response to ppb level concentrations of formaldehyde.

## Adsorption kinetics study

It is well known that adsorption plays a very important role in gas sensing processes. To further investigate the selectivity of SNG-2 to different gases, the adsorption kinetics were studied. The adsorption curves at different temperature were firstly fitted and the adsorption rate constant was obtained. Then the adsorption activation energies to different gases can be calculated according to the Arrhenius eqn (1).[46–48]

$$k = A\exp(-E_a/RT) \quad (1)$$

$A$ is the frequency factor, $R$ is the ideal gas constant 8.314 J mol$^{-1}$ K$^{-1}$, and $T$ is the temperature in Kelvin. The activation energy is calculated from the slope of the linear plot of ln$k$ *versus* the inverse of the temperature. The higher the activation energy value, the more difficult for the material to adsorb the gas. Fig. 5 shows the adsorption curves of SNG-2 to formaldehyde, ethanol, acetone and ammonia saturated vapor, respectively. Generally, most of the adsorption isotherms follow Langmuir's mode. The corresponding adsorption kinetics data are listed in Table 2. It is obvious that the adsorption activation energy of SNG-2 to formaldehyde is significantly lower than the others. It also proves that SNG-2 has the strongest adsorption affinity for formaldehyde molecules.

## Formaldehyde sensing mechanism

$SnO_2$ is known as a typical n-type gas sensing semiconductor that exhibits high sensitivity, fast response and good stability to numerous type of gases. When it is composited with graphene or its derivatives, the sensing performance is generally further enhanced.[17,18] In this work, the SNG heterogeneous material with high content of hydrogenated pyridinic-N moiety shows high selectivity to ppb level formaldehyde with good anti-interference capability. Such excellent sensitivity is attributed to the unique microstructure of SNG.

First of all, the introduction of NGO reduces the average particle size of $SnO_2$,[14] which makes the material have a larger


© 2022 The Author(s). Published by the Royal Society of Chemistry

Open Access Article. Published on 26 May 2022. Downloaded on 2/8/2026 1:01:11 PM.
This article is licensed under a Creative Commons Attribution-NonCommercial 3.0 Unported Licence.

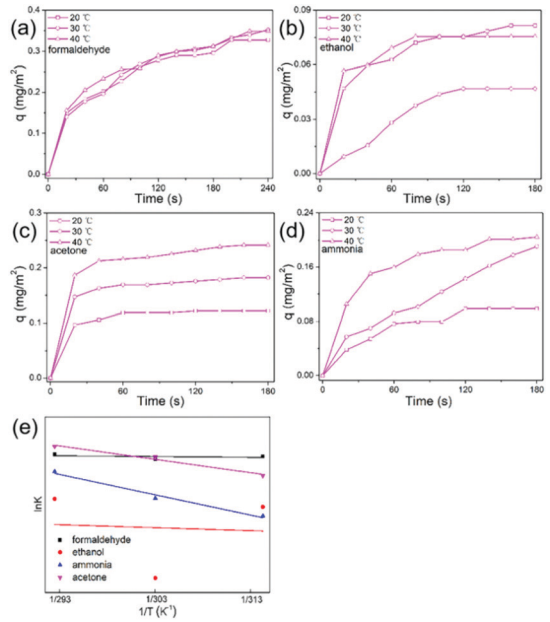


Fig. 5 Adsorption curves of the SNG-2 sensing material to (a) formaldehyde, (b) ethanol, (c) acetone and (d) ammonia vapor at different temperatures, and (e) Henry adsorption isotherms.

Table 2 Adsorption kinetics data of SNG-2 towards different gas molecules

| Gas | $T$ (K) | $k^* \ 10^{-3}$ (mg m$^{-2}$ s$^{-1}$) | In$k$ | $k^*$ | $E_a$ (J mol$^{-1}$) |
|---|---|---|---|---|---|
| Formaldehyde | 293 | 7.79 | −4.855 | −177.6 | 1477.3 |
| | 303 | 7.02 | −4.959 | | |
| | 313 | 7.48 | −4.895 | | |
| Ethanol | 293 | 2.83 | −5.867 | −680.0 | 5653.8 |
| | 303 | 0.47 | −7.665 | | |
| | 313 | 2.35 | −6.053 | | |
| Ammonia | 293 | 5.27 | −5.246 | −4641.7 | 38591.4 |
| | 303 | 2.86 | −5.857 | | |
| | 313 | 1.91 | −6.261 | | |
| Acetone | 293 | 7.36 | −4.912 | −3051.2 | 25368.3 |
| | 303 | 9.34 | −4.673 | | |
| | 313 | 4.81 | −5.337 | | |

specific surface area and a stronger ability to adsorb gases.[15] Furthermore, plenty of mesospheres formed within the material provide a favorable framework for electron and gas transport.[22,25,49–51] This may facilitate the mass transfer and accelerate the sensing response speed. If only taking into account the response value per unit specific surface area, the SG samples exhibit the greatest sensitivity. However, the overall sensing response and selectivity is not as satisfactory as that of SNG-2. So there should be other important factors for improving formaldehyde sensitivity.

Secondly, the hydrogenated pyridinic-N moiety from NGO plays a vital role in promoting selective adsorption and catalyzing sensing reactions.[26] N-doping can effectively change the spin density and charge distribution of the conjugated network.[27,52–54] Compared to the C atom, N has one more valence electron. So N-doping results in some content of positively charged C and negatively charged N in NGO. It can create different adsorption sites for gases with different electronegativity. In the doped C–N conjugated structure of NGO, the C atom has partial positive charge and tends to adsorb $O_2$.[27,28] Different N-doping structures will affect the adsorption of oxygen by adjacent C. There are mainly four types of N-doped moieties in our SNG materials: graphitic-N, pyridinic-N, pyrrolic-N and hydrogenated pyridinic-N. The C next to graphite N has very weak positive charge, and the adsorbing oxygen effect is relatively poor. Hydrogenated pyridinic-N can give rise to the chemisorbed state of molecular oxygen on their laterally adjacent carbon atoms because of the strong positive charge.[27,28,53,54] However, pyridinic-N or pyrrolic-N may induce too much electropositivity for the C atom and the $O^-$ adsorption is too strong. Therefore, it is difficult for $O^-$ to react and remove from the material surface, which weakens the sensing effect. While positive C in NGO adsorbs oxygen, formaldehyde is adsorbed around negative N. So the concentration of adsorbed $O^-$ and HCHO molecules on the SNG surface increases significantly. The orderly staggered distribution facilitates the subsequent sensing reactions between the two species. Therefore, the SNG with a high content of active adsorption sites could adsorb the target molecules more accurately under very low concentrations of target gas. In addition, the high selectivity and good anti-interference of SNG are speculated to be related to the hydrogenated pyridinic-N structure. In previous works, if a mixture of many substances is used as the target vapor, it is generally difficult for the sensor to distinguish one (*e.g.*, HCHO) from the others, because of their similar sensing mechanism. However, the as-prepared SNG shows high anti-interference to ethanol, acetone and ammonia. This is also attributed to the high content of hydrogenated pyridinic-N moieties. Because the electric affinity and steric hindrance of graphitic-N, pyridinic-N, pyrrolic-N and hydrogenated pyridinic-N are different from each other. Gas molecules only with the most matching electronic structure and molecular size can be selectively adsorbed. It is supposed that SNG-2 has a high content of hydrogenated pyridinic-N moieties, which provides the most favorable microstructure for formaldehyde sensitivity. The relevant selection mechanism needs to be further studied.

Thirdly, the hydrogenated pyridinic-N moiety is considered to be an important structure for catalyzing the formaldehyde sensing process. Generally, hydrogenated pyridinic-N atoms are predominantly formed on the edges of defect sites in the graphene plane, as shown in Fig. 3(f). Such carbon atoms at armchair edges of the graphite material are much more active than those within the plane of graphene. It is believed that this unique doping structure create some activated regions on the graphene surface,[27,28,55] resulting in enhanced adsorption and reactive intermediates that proceed to accelerate the oxygen reduction reactions. Considering that the formaldehyde sensing process is based on the redox reaction,[56,57] it can be reasonably speculated that hydrogenated pyridinic-N plays an important catalytic role in the formaldehyde sensing process. According to the XPS analysis, we supposed that SNG-2 has a high content of hydrogenated pyridinic-N dopants at armchair

Open Access Article. Published on 26 May 2022. Downloaded on 2/8/2026 1:01:11 PM.
This article is licensed under a Creative Commons Attribution-NonCommercial 3.0 Unported Licence.

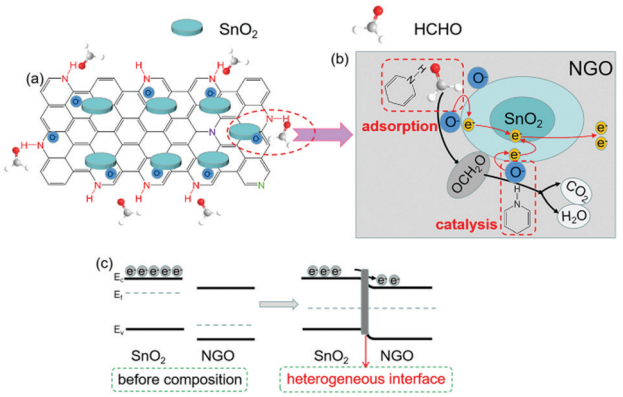


Fig. 6 Schematic diagram of (a) selective adsorption of $O_2$ and HCHO by SNG-2, (b) catalytic effect by SNG-2, and the (c) band structure of the heterogeneous interface.

edges of graphene. This N-doped structure can give monodentate activation to selective chemisorption and chemical reactions between $O^-$ and HCHO.

Finally, the heterogeneous interface takes part in enhancing the sensing performances. The addition of NGO to $SnO_2$ can effectively change the valence band structure, by increasing π electron density near the Fermi level and reducing the performance function.[52,53,58] The impedance test (Fig. S2, ESI†) proved that after composition of $SnO_2$ with NGO, the resistance of the heterogeneous material is significantly reduced. This implies that the material interface improves the separation and conduction of carriers, and the sensitivity is greatly enhanced. The energy band structure of SNG and the corresponding carrier migration process are shown in Fig. 6.

In summary, when the SNG-2 is exposed to the air, oxygen molecules are firstly adsorbed on the surface, and transfer into oxygen ions ($O_2^-$ and $O^-$) at the optimal working temperature of 160 °C, shown as formula (2), (3) and (4).[29]

$$O_2\ (gas) \rightarrow O_2\ (ads) \quad (2)$$

$$O_2\ (ads) + e^- \rightarrow O_2^-\ (ads) \quad (3)$$

$$O_2^-\ (ads) + e^- \rightarrow 2\ O^-\ (ads) \quad (4)$$

With the chemical adsorption of oxygen, formaldehyde molecules are selectively adsorbed around $O^-$ because of the activated regions from the hydrogenated pyridinic-N structure. Then, the HCHO molecules react with $O^-$ under the catalysis of the hydrogenated pyridinic-N to produce $CO_2$ and $H_2O$ efficiently.[56,57] The electrons captured by $O^-$ are released, causing the resistance of the material to decrease.

$$HCHO + O^- \rightarrow OCH_2O + e \quad (5)$$

$$OCH_2O + O^- \rightarrow CO_2 + H_2O + e \quad (6)$$

The change of the electrical signal is manifested as the response of the sensing material. During the sensing process, the heterogeneous interface promoted the transport of carriers significantly. Owing to the high content of hydrogenated pyridinic-N structure and uniformly distributed heterojunctions, the SNG-2 exhibits excellent selectivity and sensitivity to formaldehyde, which is applicable for ultra-sensitive formaldehyde gas detection.

## Conclusions

In this work, the $SnO_2$/NGO heterogeneous material with a high content of hydrogenated pyridinic-N moiety was prepared by a hydrothermal method using a mixture of urea and $NH_3{\cdot}H_2O$ as the nitrogen doping reagent. The material exhibits high response and good linearity at a formaldehyde concentration of 100–1000 ppb and 1–10 ppm. It also shows high selectivity to formaldehyde and good anti-interference. The excellent performances are attributed to selective adsorption, the catalytic effect and the heterogeneous interface. This work provides a feasible method for regulating nitrogen-doped moieties in NGO, and constructing an ultrasensitive $SnO_2$/NGO material to detect formaldehyde at the ppb level.

## Conflicts of interest

There are no conflicts to declare.

## Acknowledgements

This work was financially supported by the Natural Science Foundation of Shaanxi Province (2021JM-383).

## Notes and references

1 D. Wang, K. Wan, M. Zhang, H. Li, P. Wang, X. Wang and J. Yang, Constructing hierarchical $SnO_2$ nanofiber/nanosheets for efficient formaldehyde detection, *Sens. Actuators, B*, 2018, **283**, 714–723.
2 J. X. Wang, B. Zou, S. P. Ruan, J. Zhao and F. Q. Wu, Synthesis, characterization, and gas-sensing property for HCHO of Ag-doped $In_2O_3$ nanocrystalline powders, *Mater. Chem. Phys.*, 2009, **117**, 489–493.
3 P. Lv, Z. A. Tan, J. Yu, F. T. Zhang, G. F. Wei, Z. X. Huang and Y. Hu, Study on a micro-gas sensor with $SnO_2$-NiO sensitive film for indoor formaldehyde detection, *Sens. Actuators, B*, 2008, **132**, 74–80.
4 P. Lv, Z. Tang, G. Wei, J. Yu and Z. Huang, Recognizing indoor formaldehyde in binary gas mixtures with a micro gas sensor array and a neural network, *Meas. Sci. Technol.*, 2007, **18**, 2997–3004.
5 K. Kawamura, K. Kerman, M. Fujihara, N. Nagatani, T. Hashiba and E. Tamiya, Development of a novel hand-held formaldehyde gas sensor for the rapid detection of sick building syndrome, *Sens. Actuators, B*, 2005, **105**, 495–501.
6 A. Allouch, M. Guglielmino, P. Bernhardt, C. A. Serra and S. Le Calvé, Transportable, fast and high sensitive near real-time analyzers: Formaldehyde detection, *Sens. Actuators, B*, 2013, **181**, 551–558.


© 2022 The Author(s). Published by the Royal Society of Chemistry

Open Access Article. Published on 26 May 2022. Downloaded on 2/8/2026 1:01:11 PM. This article is licensed under a Creative Commons Attribution-NonCommercial 3.0 Unported Licence.

7 N. Lavanya, C. Sekar, E. Fazio, F. Neri, S. G. Leonardi and G. Neri, Development of a selective hydrogen leak sensor based on chemically doped $SnO_2$ for automotive applications, *Int. J. Hydrogen Energy*, 2017, **42**, 10645–10655.
8 A. Tricoli, M. Graf and S. E. Pratsinis, Optimal Doping for Enhanced $SnO_2$ Sensitivity and Thermal Stability, *Adv. Funct. Mater.*, 2008, **18**, 1969–1976.
9 Y. Lin, W. Wei, Y. Li, F. Li, S. D. Zhou and S. Ruan, Preparation of Pd nanoparticle-decorated hollow $SnO_2$ nanofibers and their enhanced formaldehyde sensing properties, *J. Alloys Compd.*, 2015, **651**, 690–698.
10 Y. Li, N. Chen, D. Deng, X. Xing, X. Xiao and Y. Wang, Formaldehyde detection: $SnO_2$ microspheres for formaldehyde gas sensor with high sensitivity, fast response/recovery and good selectivity, *Sens. Actuators, B*, 2017, **238**, 264–273.
11 J. Hu, T. Wang, Y. Wang, D. Huang, G. He, Y. Han and Z. Yang, Enhanced formaldehyde detection based on Ni doping of $SnO_2$ nanoparticles by one-step synthesis, *Sens. Actuators, B*, 2018, **263**, 120–128.
12 G. Zhang, X. Han, W. Bian, J. Zhan and X. Ma, Facile synthesis and high formaldehyde-sensing performance of NiO-$SnO_2$ hybrid nanospheres, *RSC Adv.*, 2016, **6**, 3919–3926.
13 S. Shu, M. Wang, W. Yang and S. Liu, Synthesis of surface layered hierarchical octahedral-like structured $Zn_2SnO_4$/$SnO_2$ with excellent sensing properties toward HCHO, *Sens. Actuators, B*, 2017, **243**, 1171–1180.
14 X. Rong, D. Chen, G. Qu, T. Li, R. Zhang and J. Sun, Effects of graphene on the microstructures of $SnO_2$@rGO nanocomposites and their formaldehyde-sensing performance., *Sens. Actuators, B*, 2018, **269**, 223–237.
15 D. Wang, M. Zhang, Z. Chen, H. Li, A. Chen, X. Wang and J. Yang, Enhanced formaldehyde sensing properties of hollow $SnO_2$ nanofibers by graphene oxide, *Sens. Actuators, B*, 2017, **250**, 533–542.
16 K. Wan, J. Yang, D. Wang and X. Wang, Graphene Oxide@3D Hierarchical $SnO_2$ Nanofiber/Nanosheets Nanocomposites for Highly Sensitive and Low-Temperature Formaldehyde Detection, *Molecules*, 2019, **25**, 35.
17 D. Wang, L. Tian, H. Li, K. Wan, X. Yu, P. Wang and J. Yang, Mesoporous Ultrathin $SnO_2$ Nanosheets In-situ Modified by Graphene Oxide for Extraordinary Formaldehyde Detection at Low Temperature, *ACS Appl. Mater. Interfaces*, 2019, **11**, 12808–12818.
18 K. Toda, R. Furue and S. Hayami, Recent progress in applications of graphene oxide for gas sensing: A review, *Anal. Chim. Acta*, 2015, **878**, 43–53.
19 S. Kochmann, T. Hirsch and O. S. Wolfbeis, Graphenes in chemical sensors and biosensors, *Trends Anal. Chem.*, 2012, **39**, 87–113.
20 B. Xie, Y. Chen, M. Yu, X. Shen, H. Lei, T. Xie and Y. Wu, Carboxyl-Assisted Synthesis of Nitrogen-Doped Graphene Sheets for Supercapacitor Applications, *Nanoscale Res. Lett.*, 2015, **10**, 332.
21 A. K. Singh, K. C. Basavaraju, S. Sharma, S. Jang, C. P. Park and D. P. Kim, Eco-efficient preparation of a N-doped graphene equivalent and its application to metal free selective oxidation reaction, *Green Chem.*, 2014, **16**, 3024–3030.
22 Y. Yang, Z. Z. Pan, Y. Y. Wang, Y. C. Ma, C. Li, Y. J. Lu and X. L. Wu, Ionic-liquid-bifunctional wrapping of ultrafine $SnO_2$ nanocrystals into N-doped graphene networks: high pseudocapacitive sodium storage and high-performance sodium-ion full cells, *Nanoscale*, 2019, **11**, 14616–14624.
23 G. Z. Wang, J. M. Feng, L. Dong, X. F. Li and D. J. Li, $SnO_2$ particles anchored on N-doped graphene surface as sodium-ion battery anode with enhanced electrochemical capability, *Appl. Surf. Sci.*, 2017, **396**, 269–277.
24 N. Wu, W. Du, X. Gao, L. Zhao, G. Liu, X. Liu and Y. B. He, Hollow $SnO_2$ nanospheres with oxygen vacancies entrapped by a N-doped graphene network as robust anode materials for lithium-ion batteries, *Nanoscale*, 2018, **10**, 11460–11466.
25 X. Lu, G. Wu, Q. Xiong, H. Qin, Z. Ji and H. Pan, Laser in-situ synthesis of $SnO_2$/N-doped graphene nanocomposite with enhanced lithium storage properties based on both alloying and insertion reactions, *Appl. Surf. Sci.*, 2017, **422**, 645–653.
26 P. Lazar, R. Mach and M. Otyepka, Spectroscopic Fingerprints of Graphitic, Pyrrolic, Pyridinic and Chemisorbed Nitrogen in N-Doped Graphene, *J. Phys. Chem. C*, 2019, **123**, 10695–10702.
27 S. Kabir, K. Artyushkova, A. Serov and P. Atanassov, Role of Nitrogen Moieties in N-Doped 3D-Graphene Nanosheets for Oxygen Electroreduction in Acidic and Alkaline Media, *ACS Appl. Mater. Interfaces*, 2018, **10**, 11623–11632.
28 A. Ferre-Vilaplana and E. Herrero, Understanding the chemisorption-based activation mechanism of the oxygen reduction reaction on nitrogen-doped graphitic materials, *Electrochim. Acta*, 2016, **204**, 245–254.
29 A. Xu, L. Shi, L. Zeng and T. S. Zhao, First-principle investigations of nitrogen-, boron-, phosphorus-doped graphite electrodes for vanadium redox flow batteries, *Electrochim. Acta*, 2019, **300**, 389–395.
30 Z. Luo, S. Lim, Z. Tian, J. Shang, L. Lai, B. MacDonald and J. Lin, Pyridinic N doped graphene: synthesis, electronic structure, and electrocatalytic property, *J. Mater. Chem.*, 2011, **21**, 8038.
31 I. Y. Jeon, H. J. Choi, M. J. Ju, I. T. Choi, K. Lim, J. Ko and J. B. Baek, Direct nitrogen fixation at the edges of graphene nanoplatelets as efficient electrocatalysts for energy conversion, *Sci. Rep.*, 2013, **3**, 2260.
32 G. H. Jun, S. H. Jin, B. Lee, B. H. Kim, W. S. Chae, S. H. Hong and S. Jeon, Enhanced conduction and charge-selectivity by N-doped graphene flakes in the active layer of bulk-heterojunction organic solar cells, *Energy Environ. Sci.*, 2013, **6**, 3000.
33 E. T. Mombeshora, P. G. Ndungu and V. O. Nyamori, The physicochemical properties and capacitive functionality of pyrrolic-and pyridinic-nitrogen, and boron-doped reduced graphene oxide, *Electrochim. Acta*, 2017, **258**, 467–476.
34 L. Sun, L. Wang, C. Tian, T. Tan, Y. Xie, K. Shi and H. Fu, Nitrogen-doped graphene with high nitrogen level via a one-step hydrothermal reaction of graphene oxide with urea for superior capacitive energy storage, *RSC Adv.*, 2012, **2**, 4498.
35 N. W. Pu, C. Y. Chen, H. X. Qiu, Y. M. Liu, C. H. Song, M. H. Lin and M. D. Ger, Hydrothermal Synthesis of

Open Access Article. Published on 26 May 2022. Downloaded on 2/8/2026 1:01:11 PM.
This article is licensed under a Creative Commons Attribution-NonCommercial 3.0 Unported Licence.

N-Doped Graphene/$Fe_2O_3$ Nanocomposite for Supercapacitors, *Int. J. Electrochem. Sci.*, 2018, **68**, 6812–6823.

36 S. Peng, H. L. Guo and X. F. Kang, Preparation of Nitrogen-Doped Graphene and Its Electrocatalytic Activity for Oxygen Reduction Reaction, *Acta Phys.-Chim. Sin.*, 2014, **30**, 1778–1786.

37 H. M. Jeong, J. W. Lee, W. H. Shin, Y. J. Choi, H. J. Shin, J. K. Kang and J. W. Choi, Nitrogen-Doped Graphene for High-Performance Ultracapacitors and the Importance of Nitrogen-Doped Sites at Basal Planes, *Nano Lett.*, 2011, **11**, 2472–2477.

38 H. Bi, L. X. Zhang, Y. Xing, P. Zhang, J. J. Chen, J. Yin and L. J. Bie, Morphology-controlled synthesis of CeO2 nanocrystals and their facet-dependent gas sensing properties, *Sens. Actuators, B*, 2021, **330**, 129374.

39 Y. Xing, L. X. Zhang, C. T. Li, Y. Y. Yin and L. J. Bie, Pt decoration and oxygen defects synergistically boosted xylene sensing performance of polycrystalline SnO2 nanosheet assembled microflowers, *Sens. Actuators, B*, 2022, **354**, 131220.

40 W. Y. Yan, Q. Zhou, X. Chen, X. J. Huang and Y. C. Wu, C-doped and N-doped reduced graphene oxide/$TiO_2$ composites with exposed (001) and (101) facets controllably synthesized by ahydrothermal route and their gas sensing characteristics, *Sens. Actuators, B*, 2016, **230**, 761–772.

41 X. Zhou, S. Chen, J. Yang, T. Bai, Y. Ren and H. Tian, Metal-Organic Frameworks Derived Okra-like $SnO_2$ Encapsulated in Nitrogen-Doped Graphene for Lithium Ion Battery, *ACS Appl. Mater. Interfaces*, 2017, **9**, 14309–14318.

42 B. Bhangare, N. S. Ramgir, S. Jagtap, A. K. Debnath, K. P. Muthe, C. Terashima and A. Fujishima, XPS and Kelvin probe studies of $SnO_2$/RGO nanohybrids based $NO_2$ sensors, *Appl. Surf. Sci.*, 2019, **487**, 918–929.

43 C. S. Reddy, G. Murali, A. S. Reddy, S. Park and I. In, GO incorporated $SnO_2$ nanotubes as fast response sensors for ethanol vapor in different atmospheres, *J. Alloys Compd.*, 2019, **813**, 152251.

44 H. Yu, Y. Zhang, L. Dong and J. Wang, Fabricating pod-like $SnO_2$ hierarchical micro-nanostructures for enhanced acetone gas detection, *Mater. Sci. Semicond. Process.*, 2021, **121**, 105451.

45 N. Li, Y. Fan, Y. Shi, Q. Xiang, X. Wang and J. Xu, A Low Temperature Formaldehyde Gas Sensor Based on Hierarchical SnO/$SnO_2$ Nano-flowers Assembled from Ultrathin Nanosheets: Synthesis, Sensing Performance and Mechanism, *Sens. Actuators, B*, 2019, **294**, 106–115.

46 Ö. Demirbaş, M. H. Çalımlı, B. Demirkan, H. M. Alma, M. S. Nas, A. Khan, A. Asiri and F. Şen, The Kinetic Parameters of Adsorption of Enzymes Using Carbon-Based Materials Obtained from Different Food Wastes, *BioNanoScience*, 2019, **11**, 14616–14624.

47 L. Abramian and H. El-Rassy, Adsorption kinetics and thermodynamics of azo-dye Orange II onto highly porous titania aerogel, *Chem. Eng. J.*, 2009, **150**, 403–410.

48 D. Angi and F. Cakicioglu-Ozkan, Adsorption kinetics of methane reformer off-gases on aluminum based metal-organic framework, *Int. J. Hydrogen Energy*, 2020, **45**, 34918–34926.

49 W. Zhou, J. Wang, F. Zhang, S. Liu, J. Wang, D. Yin and L. Wang, $SnO_2$ nanocrystals anchored on N-doped graphene for high-performance lithium storage, *Chem. Commun.*, 2015, **51**, 3660–3662.

50 X. Lu, Controlled synthesis and lithium storage performance of $SnO_2$/N-doped graphene nanocomposites, MSC, College of Chemistry and Chemical Engineering China West Normal University, 2017.

51 M. Li, Q. Deng, J. Wang, K. Jiang, L. Shang, Z. Hu and J. Chu, In-situ gas reduction in reversible SnS-$SnO_2$@N-doped graphene anodes for high-rate and lasting lithium storage, *J. Alloys Compd.*, 2018, **769**, 1007–1018.

52 N. H. Vu, H. T.-T. Le, V. H. Hoang, V. D. Dao, H. T. Huu, Y. S. Jun and W. B. Im, Highly N-doped, H-containing mesoporous carbon with modulated physicochemical properties as high-performance anode materials for Li-ion and Na-ion batteries, *J. Alloys Compd.*, 2020, **851**, 156881.

53 C. K. Lin, Theoretical study of nitrogen-doped graphene nanoflakes: Stability and spectroscopy depending on dopant types and flake sizes, *J. Comput. Chem.*, 2018, **39**, 1387–1397.

54 C. K. Lin, Pyridine vs N-Hydrogenated Pyridine Moieties: Theoretical Study of Stability and Spectroscopy of Nitrogen-Contained Heterocyclic Aromatic Compounds and Graphene Nanoflakes, *ACS Omega*, 2018, **3**, 12312–12319.

55 J. H. Chen and H. T. Chen, Computational explanation for interaction between amino acid and nitrogen-containing graphene, *Theor. Chem. Acc.*, 2018, **137**, 176.

56 S. Tian, X. Ding, D. Zeng, J. Wu, S. Zhang and C. Xie, A low temperature gas sensor based on Pd-functionalized mesoporous $SnO_2$ fibers for detecting trace formaldehyde, *RSC Adv.*, 2013, **3**, 11823.

57 J. Jang, S. Lee, S. Choi, W. Koo, D. Kim, H. Shin and I. Kim, Heterogeneous, Porous 2D Oxide Sheets via Rapid Galvanic Replacement: Toward Superior HCHO Sensing Application, *Adv. Funct. Mater.*, 2019, **29**, 1903012.

58 Y. M. Kwon, R. Purbia, H. D. Kim, Y. S. Lee, H. Shin and J. M. Baik, Zero-dimensional Heterostructures: N-Doped Graphene Dots/$SnO_2$ for Ultrasensitive and Selective $NO_2$ Gas Sensing at Low Temperatures, *J. Mater. Chem. A*, 2020, **8**, 11734–11742.


© 2022 The Author(s). Published by the Royal Society of Chemistry